Journal of Materials Chemistry A

ROYAL SOCIETY OF CHEMISTRY

PAPER

View Article Online
View Journal | View Issue

Cite this: J. Mater. Chem. A, 2024, 12, 10329

Unlocking superior NO_2 sensitivity and selectivity: the role of sulfur abstraction in indium sulfide (InS) nanosheet-based sensors†

Gianluca D'Olimpio, [a] Danil W. Boukhvalov, *[b] Vardan Galstyan, ‡[c] Jessica Occhiuzzi,[a] Michael Vorochta, [d] Matteo Amati,[e] Zygmunt Milosz, [e] Luca Gregoratti,[e] Marian Cosmin Istrate,[f] Chia-Nung Kuo,[g] Chin Shan Lue,[g] Corneliu Ghica,[f] Elisabetta Comini [c] and Antonio Politano *[a]

To advance gas sensor technologies, it is essential to identify materials that exhibit both high selectivity and sensitivity. Here, we unravel the gas-sensing capabilities of indium sulfide (InS) nanosheets, particularly in relation to nitrogen dioxide (NO_2) detection. Utilizing a synergistic approach that combines *in situ* and *operando* experimental methodologies with density functional theory calculations, we demonstrate that these nanosheets offer outstanding sensitivity toward NO_2, characterized by a remarkably low detection threshold of 180 ppb at an operational temperature of 350 °C. This remarkable sensitivity is ascribed to the electronic charge redistribution around the Fermi level, facilitated by an oxygen-deficient In_2O_{3-x} surface layer that forms naturally when the InS surface is exposed to ambient conditions. A pivotal aspect of our investigation was the exploration of the influence of sulfur abstraction on these surface modifications. We demonstrate that sulfur abstraction plays a critical role in the formation and operational efficacy of the In_2O_{3-x} layer, thereby acting as a key element in the sensor mechanism. This unique surface chemistry not only amplifies the sensitivity to NO_2 but also confers unparalleled selectivity over other gases and volatile organic compounds. Notably, this level of performance exceeds that of other 2D semiconductors and metal oxides, thus establishing InS nanosheets as an ideal platform for high-performance gas sensors suitable for demanding environments. Moreover, unlike many state-of-the-art sensor materials, InS-based sensors can withstand a wider variety of environmental conditions due to their superior water adsorption resistance.

Received 25th February 2024
Accepted 11th March 2024

DOI: 10.1039/d4ta01287a

rsc.li/materials-a

1 Introduction

In the contemporary era, characterized by rapid industrial development and the intensifying consequences of climate change, there is an urgent need for effective air quality monitoring. As a response to this exigency, chemoresistive gas sensors, primarily based on metal-oxide semiconductors,[1–6] have been widely embraced for their compactness, user-friendly operational mechanisms, and their proficiency in detecting variations in electrical properties of metal oxides when gas molecules adsorb on their surfaces.[1,7–11] Chemoresistive sensors operate on the principle that the electrical properties of metal oxides undergo measurable changes when gas molecules are adsorbed onto their surfaces. However, the path to optimized gas detection is fraught with several challenges. Specifically, the issues of ensuring high sensitivity, optimizing sticking coefficients, and effectively managing conductance variations continue to be challenging barriers that inhibit the selectivity and sensitivity. These persistent hurdles underscore the imperative need for the development and implementation of innovative functional materials tailored to meet the unique demands of state-of-the-art gas sensing.

Recently, the focus has significantly shifted towards 2D semiconductors, which are earning recognition for their large surface areas, exceptional charge transport characteristics, and

[a]Department of Physical and Chemical Sciences, University of L'Aquila, Via Vetoio, 67100 L'Aquila, AQ, Italy. E-mail: antonio.politano@univaq.it

[b]College of Science, Institute of Materials Physics and Chemistry, Nanjing Forestry University, Nanjing 210037, P. R. China. E-mail: danil@njfu.edu.cn

[c]Sensor Lab, Department of Information Engineering, University of Brescia, Via Valotti 9, 25133 Brescia, Italy

[d]Faculty of Mathematics and Physics, Charles University, V Holešovičkách 2, Prague 8, 18000 Prague, Czech Republic

[e]Elettra – Sincrotrone Trieste SCpA, AREA Science Park, Strada Statale 14 km 163.5, 34149, Trieste, Italy

[f]National Institute of Materials Physics, Atomistilor 405A, 077125 Magurele, Romania

[g]Department of Physics, National Cheng Kung University, 1 Ta-Hsueh Road, 70101 Tainan, Taiwan

† Electronic supplementary information (ESI) available. See DOI: https://doi.org/10.1039/d4ta01287a

‡ Present address: Istituto dei Materiali per l'Elettronica ed il Magnetismo, Consiglio Nazionale delle Ricerche, Parco Area delle Scienze, 37/A Parma, 43124, Italy.

unique surface physicochemical properties.[12–21] Despite their potential, their performance has not yet reached the levels exhibited by metal oxides in terms of their sensitivity, selectivity, response/recovery time, and long-term stability. Consequently, further exploration of a wide atlas of 2D semiconductors for gas sensing is warranted.

Indium sulfide (InS) has a direct bandgap and can exist in several phases, each with distinct electronic and structural properties. Its surface properties inhibit the physisorption of oxygen, carbon monoxide, and carbon dioxide, rendering it resistant to oxidation and CO poisoning.[22–25] Previously, it was suggested to be a promising material for nonlinear optics[26] and photovoltaics.[27]

Here, we validate InS as a promising platform for the detection of noxious gases by fabricating innovative gas sensors from solution-processed InS nanosheets,[28,29] exhibiting exceptional selectivity and sensitivity for NO_2 detection, with a detection limit of 180 ppb at 350 °C.

By combining several *in situ* and *operando* spectroscopic and microscopic tools with theoretical calculations, we investigated the underlying mechanisms that contribute to the selective sensing characteristics of InS nanosheets. We focus on how surface modifications, particularly the formation of an oxygen-deficient In_2O_{3-x} native oxide skin, and electronic charge redistribution play a pivotal role in the sensing capabilities of InS-based sensors. Moreover, we assessed the effects of relative humidity (RH) on the NO_2 sensing capabilities of InS, a crucial aspect often overlooked in sensor development. Given that RH can significantly affect sensor performance, understanding its role is essential for real-world applications in which humidity variations are commonplace. Additionally, we scrutinized the sensor performance against that of other gaseous compounds and volatile organic compounds (VOCs) to confirm selectivity. Our research is further supported by theoretical calculations of the differential enthalpy and Gibbs free energy of adsorption for different gases, providing insights into the mechanistic aspects governing the selective response of the sensor. Our findings showcase the promise of InS as a functional material for gas-sensing applications and reinforce the importance of further investigation into 2D semiconductors to address modern gas-sensing challenges.

2 Results and discussions

2.1 Atomic structure

InS is a semiconductor belonging to the III–VI family, similar to its parental compounds GaS, GaSe, and InSe.[30–37] Like its counterparts, InS has tetrahedral coordination geometry with its constituent atoms. What distinguishes InS is its asymmetrical atomic layering: specifically, two sulfur atoms and one indium atom exist in a single plane, with an additional sulfur atom in an adjacent layer (Fig. 1a and b). The unique three-dimensional network structure of InS requires sophisticated characterization. Raman spectroscopy serves as an invaluable tool in this context, particularly for assessing stoichiometry and intra-domain variations.[38–40] In Fig. 1c, we show the room-temperature Raman spectrum of InS, and it is noteworthy that our mode assignments are in close agreement with the findings reported in the literature.[40,41] Our analysis specifically targets the most prominent A_g intralayer optical modes (A_g^1, A_g^2, A_g^4), characterized by frequencies of 150, 222, and 317 cm^{-1}. In the A_g^1 and A_g^2 modes, atomic oscillations occur parallel to the direction of the bond stretching, whereas the A_g^4 mode involves the bending vibrations of the atoms.[40,42] These vibrational modes not only offer insights into the material properties but also bear relevance to an ongoing debate about the atomic structure of InS. In fact, previous research has posited either a monoclinic or orthorhombic structure for equiatomic InS.[43] To clarify this, we performed a single-crystal X-ray diffraction (XRD) analysis. The resulting lattice parameters $a = 4.45$ Å, $b = 10.65$ Å, $c = 3.94$ Å, and $\alpha = \beta = \gamma = 90°$ corroborate an orthorhombic structure, as indexed according to CIF file no. 1540925. Fig. 1c displays the Laue diffraction pattern of the bulk crystal, further confirming orthorhombic symmetry through cleavage along the (010) plane. Supplementing these insights from spectroscopic and diffraction tools, Fig. 1e shows a high-resolution TEM (HRTEM) micrograph of the [100] zone axis orientation. The small-area electron diffraction (SAED) pattern in Fig. 1f confirms this orientation, with the [010] direction oriented towards the crystal border and the [001] direction parallel to it. An overlay of the InS unit cell atomic model onto the HRTEM image (inset of Fig. 1e) offers additional validation. Notably, the exterior border of the grain reveals a marked difference in the HRTEM pattern owing to the native oxide layer formed upon exposure to air, which is further corroborated by the low oxygen peak in the EDS spectrum (Fig. S2 in the ESI†).

2.2 Chemical reactivity and surface oxidation

Having characterized the structural attributes of InS using a diverse array of experimental techniques, we subsequently turned our attention to a theoretical exploration of its surface properties. Our model focuses on the adsorption dynamics of various small molecules, namely O_2, H_2, H_2O, CO, CO_2, NO_2, C_2H_6O (ethanol), and C_3H_6O (acetone), in both the bulk and monolayer configurations of InS. For the bulk structure, a $4 \times 4 \times 2$ supercell slab was employed, and only the atomic positions were optimized to accurately represent the surface and subsurface regions. In contrast, the monolayer configuration underwent comprehensive optimization, including adjustments to both atomic positions and lattice parameters. The results of these calculations, as detailed in Table 1, reveal that physisorption is thermodynamically viable for all considered molecular species, even at elevated temperatures up to 400 °C (see Fig. 2a), that is, the standard operational temperature of state-of-the-art gas sensors.

The calculated differential Gibbs free energies for physisorption at 400 °C are all below −70 kJ mol^{-1}. The monolayer of InS displays analogous adsorption behavior, with the notable exception of hydrogen at 400 °C, where the process is unfavorable ($\Delta G = +17.9$ kJ mol^{-1}, as outlined in Table 1). The establishment of robust non-covalent bonding is associated with relatively short (about 0.24–0.27 nm) separations between

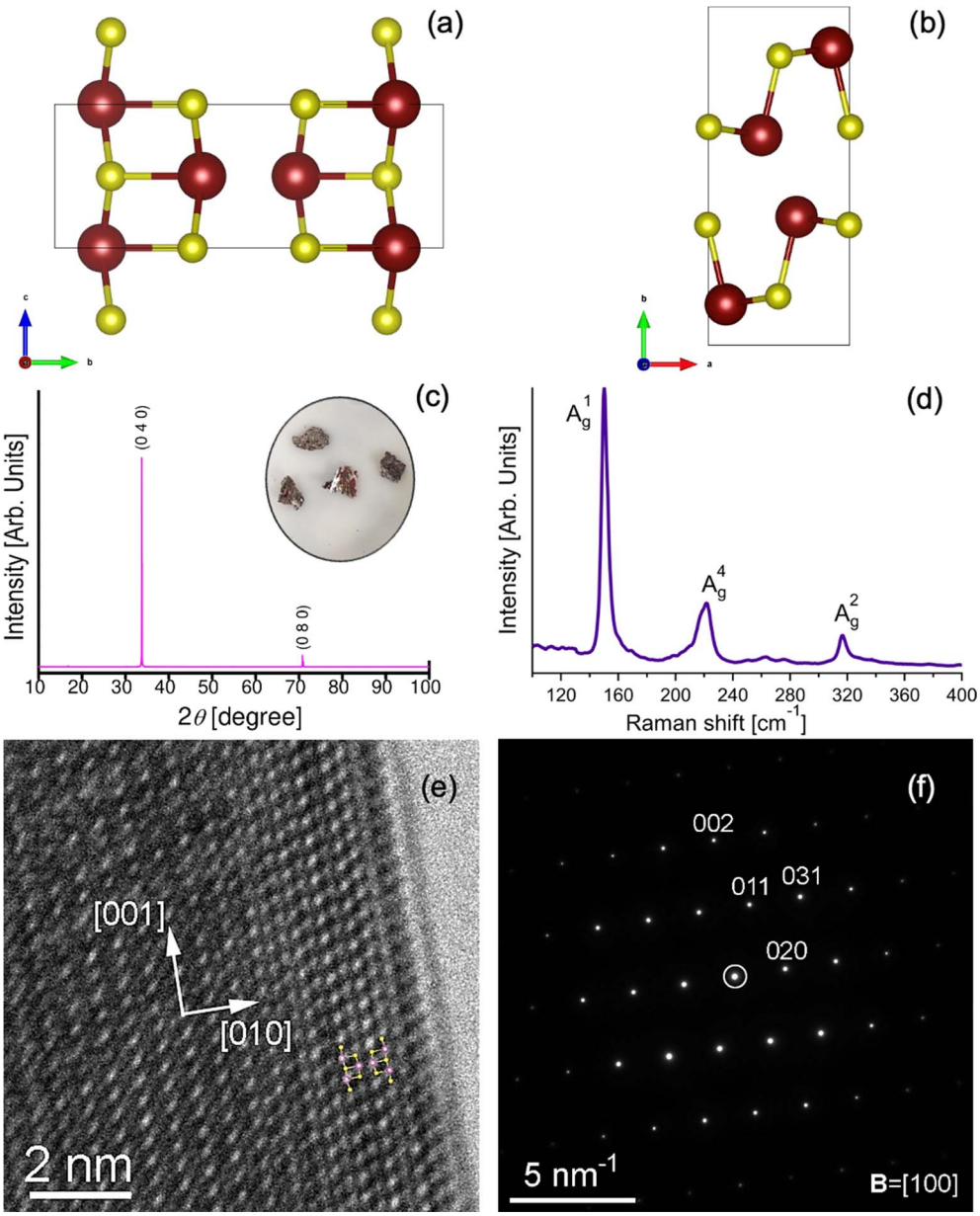

Fig. 1 The orthorhombic atomic structure of InS projected along the (a) [100] and (b) [001] directions, respectively. Brown and yellow spheres denote In and S, respectively. (c) XRD pattern of as-cleaved InS bulk single crystal; (d) Raman spectrum of the InS single-crystal acquired at room temperature with $\lambda = 532$ nm. (e) and (f) HRTEM image and associated SAED pattern, respectively, from a thin area at the border of an InS grain in the [100] orientation. The inset in (e) shows an atomic structural model of the InS unit cell in the [100] crystallographic orientation.

analytes and substrates. As seen in Fig. 2b, the integration of small diatomic and triatomic molecules into surface cavities is made possible by the distinct atomic architecture of InS. For all the examined diatomic and triatomic molecules, with the exception of CO, migration from the surface into these cavities is an exothermic process, characterized by differential enthalpies of incorporation below -65 kJ mol^{-1}. Consequently, the unaltered surface of InS did not exhibit selective adsorption; rather, it was highly receptive to a broad range of molecular species.

After the initial oxygen incorporation into the InS surface, two viable scenarios emerged. First, oxygen atoms integrate into the surface, culminating in the formation of an In_2S_2O surface layer, as depicted in Fig. 2c. The energetics associated with the formation of this structure register at an energy of -252 kJ per O_2 molecule, strongly suggesting that this transition to an oxidized state is energetically advantageous. Therefore, the likelihood of encountering such an oxidized layer is significant. Computational evaluations were performed to study the physisorption behavior of specific molecular species on an oxidized In_2S_2O surface. The data revealed that oxidation of the InS surface led to a marked increase in selectivity towards adsorption. Specifically, at an operational temperature of 400 °C, only hydrogen, ethanol, and acetone achieved thermodynamically stable adsorption states, with ΔG values falling below -50 kJ mol^{-1}.

Table 1 The calculated differential enthalpy and Gibbs free energies of physisorption (see Fig. 2) at 400 °C for various gases on pristine bulk and monolayer InS and its oxidized surface (In_2S_2O, Fig. 2c). The differential enthalpies for the incorporation of physisorbed molecules into the cavities (grooves) on the surface of InS (see Fig. 2b)

Analyte	ΔH, kJ mol^{-1}	ΔG (400 °C), kJ mol^{-1}
InS (bulk surface)		
O_2	−455.1 (−384.8)	−429.2
H_2	−251.3 (−101.4)	−232.6
H_2O	−375.7 (−97.9)	−305.0
CO	−381.6 (+16.5)	−337.9
CO_2	−106.6 (−65.8)	−70.3
NO_2	−531.4 (−123.0)	−456.7
Ethanol	−393.2	−337.7
Acetone	−391.2	−317.8
InS (monolayer)		
O_2	−268.5 (−257.6)	−242.6
H_2	−0.8	+17.9
H_2O	−117.4	−46.7
CO	−93.1	−49.4
CO_2	−171.3	−135.0
NO_2	−286.7	−212.0
Ethanol	−132.8	−77.3
Acetone	−106.4	−33.0
In_2S_2O		
H_2	−81.8	−63.1
H_2O	−16.8	53.9
CO	−30.4	13.3
CO_2	−16.4	19.9
NO_2	−36.7	38.0
Ethanol	−100.4	−44.9
Acetone	−126.1	−52.7

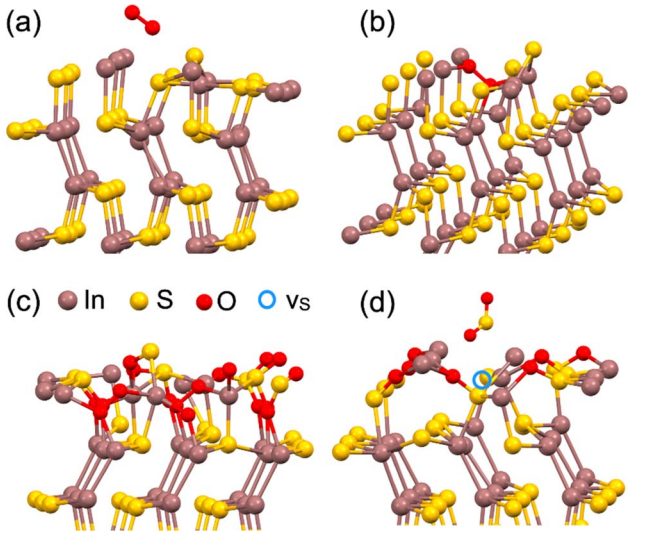

Fig. 2 (a) Optimized atomic structure of oxygen molecules physisorbed on the surface of bulk InS and (b) further incorporation into the interstitial spaces on the surface. (c) The subsequent formation of an oxidized In_2S_2O layer and (d) the further extraction of sulfur atom *via* release of SO_2 molecule, resulting in the formation of a sulfur vacancy (v_s).

The second scenario considers the volatile nature of oxidized sulfur atoms, recognizing that the liberation of SO_2 gas and formation of sulfur vacancy (v_S) is probable in sulfur-based materials, as depicted in Fig. 2d. Two possible pathways were formulated in this scenario. The resultant localized atomic configuration was successfully captured using the empirical formula $In_4S_4O_2$. Subsequent developments in these pathways are represented by the following chemical equations:

$$In_4S_4O_2 \rightarrow In_4S_3 + SO_2, \quad (1)$$

$$In_4S_4O_2 + \tfrac{1}{2}O_2 \rightarrow In_4S_3O + SO_2. \quad (2)$$

Both situations are more energetically favorable than the formation of the In_2S_2O surface. Precisely, the calculated differential enthalpies for these reactions were approximately −320 and −550 kJ mol^{-1} for the bulk and monolayer configurations, respectively. Further release of additional SO_2 molecules, mediated by reactions analogous to those previously described, also emerges as an energetically favorable process, featuring associated differential enthalpies below −300 kJ mol^{-1}. These processes result in a systematic depletion of sulfur atoms from the surface layer, while concomitantly forming a layer rich in metallic indium. Given the established susceptibility of pure indium to oxidation when exposed to ambient air,[44] the rapid and spontaneous formation of a surface In_2O_3 layer should be considered an inescapable outcome, even during brief periods of air exposure. To extend our analysis, we also considered the interaction of the NO_2 molecule with the InS surface. The computational results show that the reaction that follows when the SO_2 molecule is released is endothermic, but the energy barrier is only slightly larger than that, at about +36 kJ mol^{-1}. As a result, we suggest that when InS interacts with species that include oxygen, its surface displays intrinsic instability. As a result, we modelled various surface topologies based on In_2O_3. Considering existing research that emphasizes the relationship between the sensing capabilities of In_2O_3-based systems and the quality of their surfaces,[45–49] we examined three distinct variations of the (111) surface of In_2O_3. Furthermore, considering the SO_2 released as a result of the indium framework breaking down during oxidation, as mentioned in the previous section, we extended our simulations to incorporate sub-stoichiometric configurations (In_2O_{3-x}). Note that exposure of oxidized InS at 400 °C can also increase number of oxygen vacancies. The potential influence of substrate-induced strain was also considered in this context.

Initially, we employed a model of an In_2O_3 slab that uses lattice parameters corresponding to bulk indium oxide, focusing solely on optimizing atomic positions. This serves as a representative model for the formation of a dense In_2O_3 layer with an atomic arrangement that approaches the ideal. The computational results for this rigid In_2O_3 configuration revealed stable adsorption states for hydrogen, acetone, and ethanol molecules at 400 °C on an oxygen-rich surface, as shown in Table 2. In contrast, the introduction of oxygen vacancies considerably amplifies the sensitivity of the material to molecular hydrogen.

Table 2 Calculated differential enthalpy and Gibbs free energies of physisorption at 400 °C for various gases on various In_2O_3-based substrates

Analyte	ΔH, kJ mol^{-1}	ΔG (400 °C), kJ mol^{-1}
In_2O_3/$In_2O_{2.83}$ (rigid)		
H_2	−62.8/−21.1	−44.1/−2.4
H_2O	−44.4/−21.9	26.3/48.8
CO	−12.8/37.1	30.9/80.8
CO_2	37.1/76.8	73.4/113.1
NO_2	9.4/−0.4	84.1/74.3
Ethanol	−98.8/−33.5	−43.3/22.0
Acetone	−102.3/7.5	−28.9/80.9
In_2O_3/$In_2O_{2.83}$ (flexible)		
H_2	−60.1/9.8	−41.4/28.5
H_2O	−2.1/85.1	68.6/155.8
CO	32.2/81.4	75.9/125.1
CO_2	51.4/155.8	87.7/155.8
NO_2	63.9/4.3	138.6/79.0
Ethanol	−77.4/−129.2	−21.9/−34.9
Acetone	−61.7/−74.9	11.7/−1.5
In_2O_3/$In_2O_{2.83}$/$In_2O_{2.67}$ (strained rigid)		
H_2	−48.4/−27.0/−57.1	−29.7/−8.3/−38.4
H_2O	−29.9/−0.3/−35.0	40.8/70.4/35.7
CO	2.7/13.5/4.5	46.4/57.2/48.2
CO_2	8.4/23.3/16.1	44.7/59.6/52.4
NO_2	−24.1/−97.0/−123.7	50.6/−22.3/−49.0
Ethanol	−52.7/−115.7/−96.9	2.8/−60.2/−41.4
Acetone	−77.2/−103.2/−97.0	−3.8/−29.8/−23.6

Our subsequent set of computational simulations involved the comprehensive optimization of both the atomic positions and lattice parameters in the In_2O_3 surface layer. This model portrays a flexible material layer characterized by weak substrate interactions. For this oxygen-rich, flexible configuration of In_2O_3, the computational findings are largely parallel to those observed for the rigid slab, specifically, the stable adsorption of hydrogen, acetone, and ethanol molecules. However, when we explored an oxygen-deficient flexible slab variant ($In_2O_{2.83}$), our simulations indicated that stable adsorption at 400 °C is limited exclusively to ethanol and acetone.

Next, we explored the implications of the substrate-induced strain on the surface layer of In_2O_3. The oxide layer was stretched by 7% in order to align the lattice structures and so reduce the lattice mismatch between the In_2O_3 surface layer (whose in-plain lattice parameter was equal to 1.20 Å for the (111) surface) and the InS substrate (whose in-plain lattice parameter was 1.31 Å). Fixed lattice parameters were used in atomic structure optimization to mimic the effect of a stiff substrate on the surface layer.

Our computational evaluation of this strain-engineered rigid In_2O_3 slab reveals a landscape conducive to the stable adsorption of molecular hydrogen in an oxygen-rich milieu. The adsorption of the other species under examination is either unfavorable or resides in metastable states. Importantly, the introduction of oxygen vacancies into the material creates favorable conditions for the adsorption of H_2, NO_2, ethanol, and acetone. The reduced

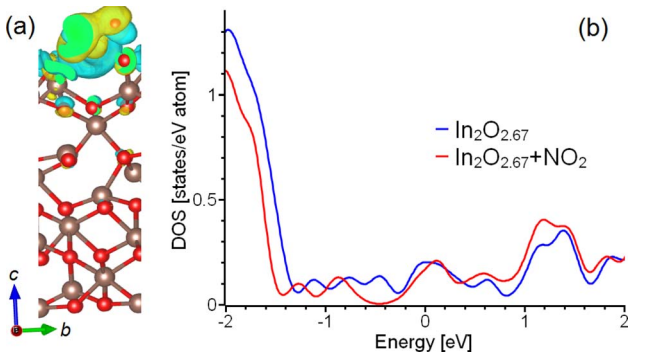

Fig. 3 (a) Charge density redistribution after adsorption of NO_2 on strained $In_2O_{2.67}$ surface. (b) Densities of states of the $In_2O_{2.67}$ surface before and after NO_2 adsorption. Cyan clouds on panel (a) correspond to decreasing charge density and yellow with increasing. The Fermi level in panel (b) is set to zero.

oxygen content, represented by the $In_2O_{2.67}$ surface, appears to be especially favorable for NO_2 adsorption relative to other molecular entities. To evaluate the selectivity of NO_2 adsorption on $In_2O_{2.67}$ substrate at 400 °C, we calculated the Boltzmann distribution for the mixture of considered gases. The results of calculations (ESI, Fig. S5†) show that at 400 °C, NO_2 adsorption is more advantageous than ethanol by more than three times and hydrogen by more than six times.

Further computational investigations highlight considerable electronic restructuring in both the surface and subsurface layers. Nitrogen dioxide adsorption is accompanied by a charge redistribution in the underlying layers of $In_2O_{2.67}$ substrate (Fig. 3a). The doping of $In_2O_{2.67}$ substrate by adsorbed NO_2 leads to visible changes in electronic structure in the regions proximal to the Fermi level, as shown in Fig. 3b. These observations substantiate the argument that the heightened selectivity observed in InS-based sensors can be attributed to the emergence of oxygen-deficient In_2O_{3-x} surface layers that effectively interact with the underlying InS substrate.

Additionally, our simulations indicate the cooperative effects of water molecules and nitrogen dioxide during the adsorption process. Specifically, the presence of a water molecule in proximity to a NO_2 molecule reduces the differential Gibbs free energy of NO_2 adsorption by approximately −3 kJ mol^{-1}. This suggests that atmospheric humidity can potentially enhance the capability of the system to sense NO_2. However, it is crucial to be a factor in the role of environmental oxygen. Our computational studies revealed that the differential Gibbs free energy for the adsorption of molecular oxygen on the $In_2O_{2.67}$ surface at 400 °C is −17.4 kJ mol^{-1}. This places oxygen adsorption in a thermodynamically less stable state compared with the other analytes under consideration. Therefore, parameters such as environmental moisture and oxygen concentration should be considered as influential variables for understanding the complex behavior of InS-based sensing systems.

2.3 InS nanosheets

To maximize the surface area, we produced InS nanosheets through liquid-phase exfoliation,[29,50,51] with an average lateral

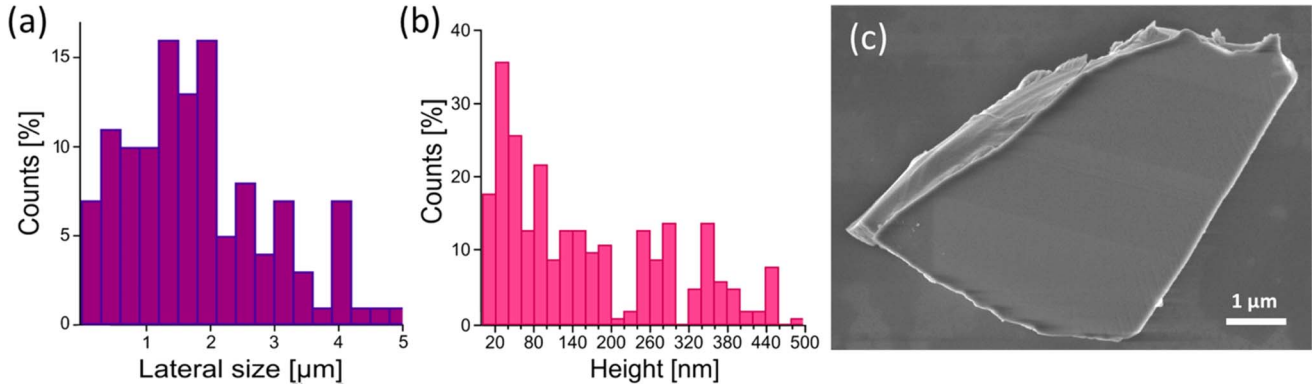

Fig. 4 Characterization of exfoliated InS nanosheets. (a) Lateral size distribution determined using an extensive dataset of SEM images. (b) Thickness distribution derived from AFM measurements. (c) SEM image showing the typical morphology of an InS nanosheet.

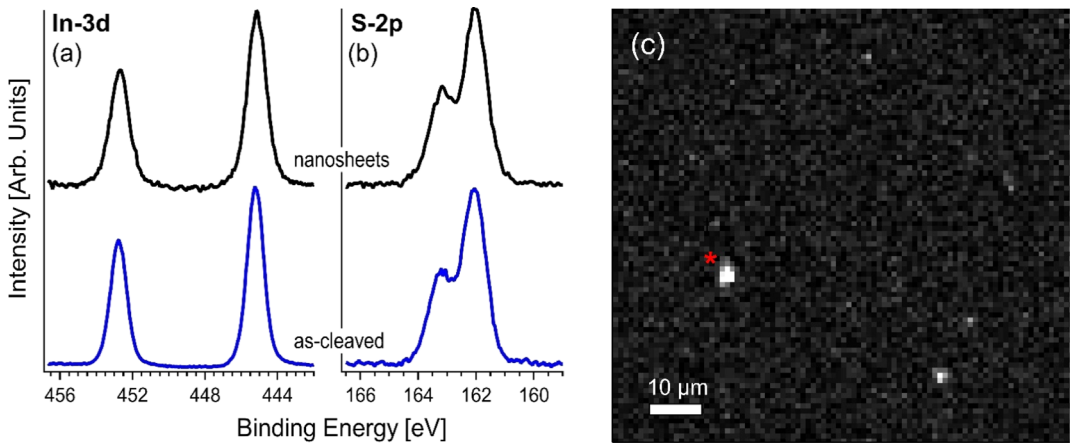

Fig. 5 XPS core level of (a) In-3d and (b) S-2p for both the as-cleaved single crystal and exfoliated InS nanosheets. (c) In-3d image of the InS nanosheets.

size of approximately 1.2 μm (see the distribution in Fig. 4a), obtained based on scanning electron microscopy (SEM) images and an average thickness of approximately 50 nm (see the distribution in Fig. 4b), obtained from atomic force microscopy, (AFM). The InS nanosheets displayed a flat surface (Fig. 4c).

XPS was employed to perform a comparative analysis between InS single crystals and exfoliated InS nanosheets, with the dual objectives of investigating possible surface modifications induced by the exfoliation process and deepening our understanding of the underlying mechanisms of gas sensing applications from the analysis of core levels. The correlation evident in the inspection of the XPS spectra (Fig. 5) of InS single crystals and nanosheets suggests surprising uniformity in their core levels. Accordingly, the exfoliation process appeared to have a minimal impact on the intrinsic physicochemical properties, thus maintaining the inherent gas-sensing functionalities of bulk InS while increasing the surface area of the nanosheets.

To deepen our understanding of the surface properties of InS nanosheets, we employed Scanning Photoelectron Microscopy (SPEM). This analytical technique provides high-resolution spatially resolved insights into the electronic structure of individual InS nanosheets. It is worth noting that the availability of spatial resolution in our XPS measurements is an invaluable asset; it offers a comprehensive perspective on the electronic landscape under operational conditions, thereby providing a pathway to decode the complex mechanisms at play in gas-sensing applications.

By shifting from surface characterization to more application-specific measurements, we conducted spatially resolved XPS studies under *operando* conditions, that replicate those experienced by the gas sensors. We focused on a particular nanosheet, identified as '*' in Fig. 5c. Initially, the exfoliated sample underwent air annealing at 350 °C, which was an essential step to fortify the adhesion of the nanosheets to the substrate while stabilizing the overall sensor assembly. Post-annealing XPS spectra (refer to Fig. 6) evidenced the emergence of a new In-3d core level component, which is interpreted as the inception of indium oxide formation.[51–54]

Interestingly, broadening of the S-2p core level was observed, which suggests the presence of indium oxide and simultaneous generation of surface defects. Nevertheless, the most intriguing phenomenon occurred when the sample was exposed to NO_2 gas at 350 °C, which is the operating temperature of the sensing devices. Evidently, NO_2 acts as a sulfur abstraction agent, essentially removing sulfur atoms from the surface, since the S-

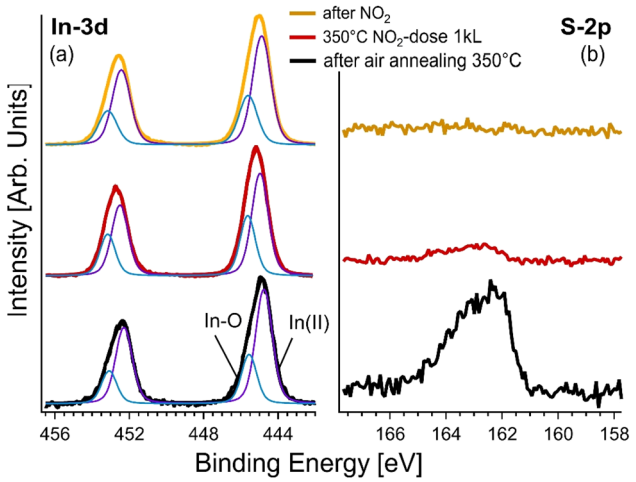

Fig. 6 *Operando* μ-XPS measurements of In-3d and S-2p core levels: (black) after air annealing at 350 °C, (red) during exposure to NO_2 gas (1 kL dose, 1 L = 10^{-6} Torr s) at 350 °C, and (yellow) after exposure to NO_2.

2p core level disappeared from the spectra in this case.[43] In contrast, the In-3d core level remained basically unaltered, underscoring the enduring presence of indium oxide on the surface.

Following exposure to NO_2, we performed an analysis of the core levels to discern the effects of gas interactions with the InS nanosheets. Of particular importance is the complete absence of the S-2p component in the XPS spectra. This was not a mere marginal reduction, but a complete elimination, providing conclusive evidence for the removal of sulfur atoms from the near-surface region probed by XPS. The absence was observed within a probing depth of approximately 2.8 nm, suggesting that the effects of NO_2 exposure were not limited to the immediate surface but extended to sub-surface layers as well. This striking result indicates that NO_2 acts not only as a passive adsorbate, but also plays an active role in altering the surface chemistry, specifically *via* sulfur abstraction.

In contrast, the In-3d core level presents a different narrative. Even after gas exposure, this component remained largely invariant in the XPS spectra. This stability is noteworthy because it indicates the resilience of the indium component of the material, even when subjected to the reactive influence of NO_2. This implies that the surface indium oxide structures, possibly formed during the initial annealing process, remain robust and unaffected by the gas–surface interactions that lead to sulfur abstraction.

The disparity in the behavior of these core levels, S-2p and In-3d, following NO_2 exposure opens avenues for further inquiries into the selectivity and sensitivity of InS-based sensors, especially considering the critical role of surface chemistry in these properties.

2.4 Gas sensing

Sensing analyses showed that the response of InS to NO_2 was enhanced as a function of its operating temperature, reaching an optimum value (response: 34.5 at 5 ppm of NO_2) at 400 °C (Fig. 7a). This behavior can be attributed to the efficient formation of oxygen vacancies by increasing the operating temperature of the material. Because NO_2 is an oxidizing gas, the presence of oxygen vacancies on the surface of the sensing structure is a crucial factor, where NO_2 molecules capture electrons acting as charge acceptors. Hence, the concentration of charge carriers on the material surface is reduced, increasing the width of the electron depletion layer, and reducing the electrical conductance of the material (Fig. 7b). Indeed, theoretical calculations have shown that the formation of an oxygen-deficient $In_2O_{2.83}$ surface is preferable for the adsorption of NO_2. Moreover, further reduction with the formation of the $In_2O_{2.67}$ surface significantly enhanced the adsorption of NO_2 on the sensor and changed its electronic structure (Table 2). In this case, the charge redistribution affects the electronic structure of the material, particularly close to the Fermi level. Thus, the experimental findings were in good agreement with our theoretical predictions. Furthermore, the dynamic response of the InS sensors to different NO_2 concentrations confirmed the n-type conductivity of the material (Fig. 7b). Fig. S1a in the ESI† shows the response variation of the InS sensor at different NO_2 concentrations in the test chamber. The response of the sensors increased with increasing NO_2 concentration, which is an important feature for quantitative analysis. The material exhibited a good sensing response to low concentrations of NO_2 with a limit of detection (LOD) of approximately 180 ppb (Fig. S1, ESI†).

We also examined the NO_2 sensing response of the fabricated sensor under dry air conditions and at 90% relative humidity (RH) in the test chamber (Fig. 7c). There was no significant difference (6.6% at 0.5 ppm of NO_2 and 7.2% for 1 ppm NO_2) between the response values at 40% RH and in dry air. The response was reduced by 34% (at 0.5 ppm NO_2) and 8.8% (at 1 ppm NO_2) when the RH concentration was increased to 90%. The adsorption of NO_2 at high RH levels was partially affected by water molecules. Water molecules can adsorb onto the sensors, inhibiting the chemisorption of the target gas. It is worth mentioning that theoretical calculations also indicate that the presence of water molecules may affect the adsorption of NO_2 on the $In_2O_{2.67}$ surface. The poor selectivity of semiconductor materials is a challenging issue for their application in conductometric gas sensing devices. Therefore, we analyzed the sensing performance of the prepared material for other gaseous and volatile organic compounds (Fig. 7d). Herein, the sensing structure showed a low response value $\left(\frac{\Delta R}{R_0} = 2\right)$ to H_2 and a weak response to acetone and ethanol ($\frac{\Delta R}{R_0}$ of 0.2 and 0.5, respectively). Furthermore, the material was not sensitive to other gaseous compounds. Thus, the proposed sensor exhibited a highly selective response to NO_2 molecules. In chemoresistive gas sensing, the adsorption of gas molecules and the transfer of electrons between the analyte molecules and the sensing structure are key factors that determine the response of the material. However, our theoretical studies considering the differential enthalpy and Gibbs free energy of the adsorption of other gases (Table 2) suggest that the formation of an oxygen-deficient surface is favorable for their detection. Thus, the excellent selective response of the material to NO_2 could be attributed to the $In_2O_{2.67}$ surface.

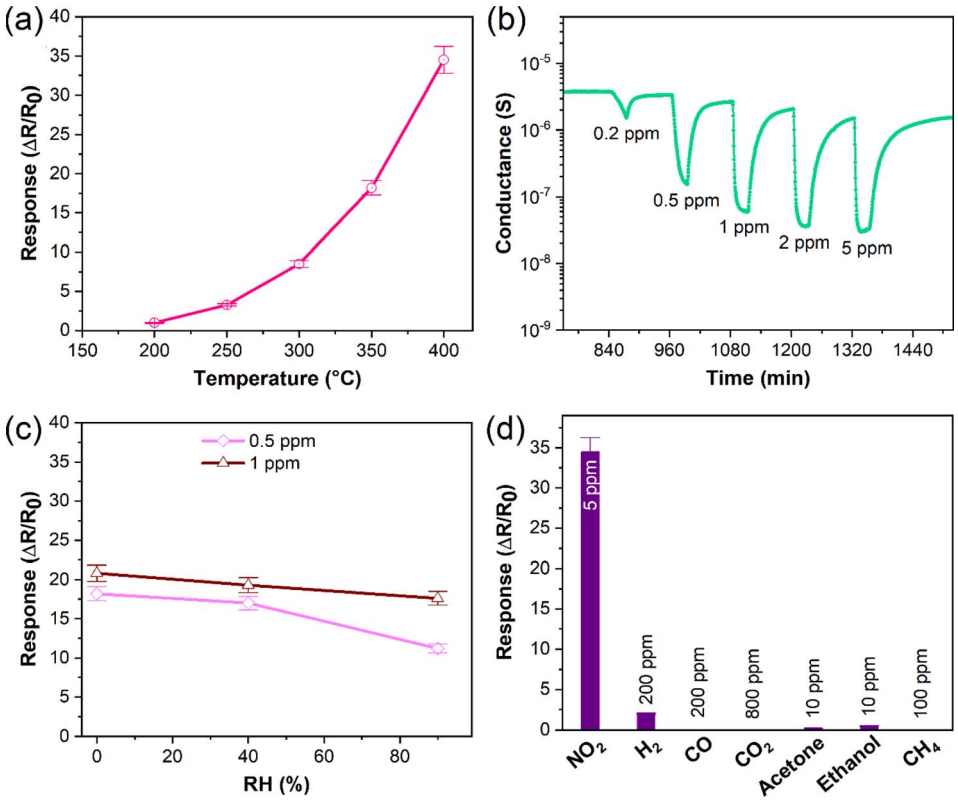

Fig. 7 (a) Response of InS towards 5 ppm of NO_2 as a function of its operating temperature (RH in the test chamber: 40%). (b) Dynamic response of InS toward different concentrations of NO_2 (0.2, 0.5, 1, 2, and 5 ppm) at 400 °C (RH, 40%). (c) Response of InS toward 0.5 and 1 ppm NO_2 as a function of RH at 400 °C. (d) Response of InS toward NO_2 (5 ppm), H_2 (200 ppm), CO (200 ppm), CO_2 (800 ppm), acetone (10 ppm), ethanol (10 ppm), CH_4 (100 ppm) at an operating temperature of 400 °C and RH of 40%. The response values for NO_2, H_2, and CO_2 were calculated as the relative variation in sample resistance ($\Delta R/R_0$). The response values for CO, acetone, ethanol, and CH_4 were calculated as the relative variation in sample conductance ($\Delta G/G_0$).

To assess the NO_2 sensing performance, we conducted a comparative analysis of InS (Table S1, ESI†) with respect to various sensors utilizing 2D semiconductors (SnS_2,[55] Sb_2Se_3,[56] N-doped In_2S_3,[57] black phosphorus,[58] and reduced graphene oxide[59]), graphitic carbon nitride,[60] metal oxides (In_2O_3 nanoparticles,[61,62] and SnO_2 nanowires[63]), and diverse heterostructures ($SnO_2/SnSe_{1.7}$,[64] In_2O_3/SnS_2,[65] SnO_2/SnS_2,[66] $SnSe_2$/SnO/SnSe,[67] and In_2O_3 nanoparticles/SnO_2 nanowires[63]). The evaluation revealed that InS outperforms state-of-the-art materials, exhibiting a superior sensing response and lower LOD than all the aforementioned systems. Additionally, while water adsorption is unfavourable on the InS surface, it is energetically favourable at near-room temperature on the surfaces of all the other above-mentioned systems. The resistance of the InS surface to water adsorption at near-room temperatures, not observed in the other materials assessed, implies a significant reduction in humidity-related interference. This characteristic could potentially lead to enhanced reliability and accuracy of NO_2 detection in real-world environments, where humidity is a variable factor.

The implications of these findings are twofold: firstly, they suggest that InS could be a leading material for developing more sensitive and reliable NO_2 sensors; secondly, the inherent resistance to water adsorption could extend the applicability of InS-based sensors to a wider range of environmental conditions, overcoming a common limitation of many current sensor materials. This research positions InS as a promising candidate for next-generation gas-sensing technologies.

3 Conclusions

In this work, we found that the superior selectivity of InS-based sensors was primarily due to the formation of an oxygen-deficient In_2O_{3-x} surface oxide layer. Our simulations showed that molecular hydrogen could be adsorbed steadily on an oxygen-rich surface, and that adding oxygen vacancies might result in very advantageous NO_2 adsorption. Although clearly less advantageous, the adsorption of H_2, ethanol, and acetone is likewise stable. Significantly, the interaction between nitrogen dioxide and the $In_2O_{2.67}$ surface leads to a substantial redistribution of charges within both the surface and subsurface layers of the substrate. This charge redistribution is particularly prominent near the Fermi level, resulting in a notable alteration of the electronic structure. Consequently, these changes contributed to the enhanced sensing capabilities of the InS nanosheets. Remarkably, our theoretical model strongly supports our experimental investigations, which clearly demonstrate alterations in surface characteristics following

sulfur abstraction. This experimental evidence effectively confirms our initial hypothesis, highlighting the pivotal role of In_2O_3 in augmenting the sensing properties of the sensor.

The implications of these findings are substantial in the field of gas sensing technology. The ability to manipulate the surface layer of the InS nanosheets could lead to the development of sensors with improved selectivity and sensitivity. Furthermore, understanding the role of charge redistribution in enhancing the sensor response opens new avenues for the design and optimization of chemoresistive gas sensors.

The InS sensor exhibits exceptional performance when benchmarked against a spectrum of current materials, including 2D semiconductors, graphitic carbon nitride, metal oxides, and various heterostructures. Noteworthy is its superior sensing response and a lower LOD, which are critical parameters in gas sensor efficiency.

Additionally, the InS surface shows a considerable decrease in interference caused by humidity as it resists water adsorption at almost ambient temperature, unlike other state-of-the-art materials for gas sensing. As a result of its inherent resistance to water adsorption, InS-based sensors could be applicable to a broader range of environmental conditions, overcoming a common limitation of many current sensor materials. Definitely, these findings imply that InS could be a leading material for developing more sensitive and reliable NO_2 sensors.

4 Methods

High-purity indium and sulfur (99.999%) were combined at a 10 : 1 molar ratio and sealed in a fused silica ampule. After heating to 810 °C for two days and gradual cooling over 10 days to 450 °C, single crystals of InS were obtained. The crystal structure at room temperature was confirmed by powder X-ray diffraction (XRD) using a Bruker D2 Phaser diffractometer equipped with Cu Kα radiation. The crystal structure orientation was determined using the Laue X-ray method.

For liquid-phase exfoliation and production of nanosheets, InS crystals were carefully pulverized in a mortar to create a fine powder. The final step was dispersing 0.03 grams of the produced InS powder in 10 milliliters of isopropyl alcohol (IPA). After that, the dispersion was exposed to a three-hour sonication procedure in a bath sonicator that was temperature-controlled to keep the temperature below 25 °C. The sample was subjected to centrifugation at 1000 rpm following sonication, which successfully separated the exfoliated flakes from any unexfoliated material. The supernatant was then gathered and ready for further examination.

A TEM sample was prepared by depositing a liquid suspension containing InS nanosheets onto a TEM grid fitted with a lacey carbon membrane. The samples were then analyzed using a JEM ARM200F TEM appatus operating at 200 kV. The observed grains, which were typically several hundred nanometers in lateral size, resulted from bulk exfoliation.

To perform gas sensing studies of the InS nanosheets, a 3 g L^{-1} dispersion of the material in isopropanol was prepared. Subsequently, platinum (Pt) interdigitated electrical contacts and a meander-shaped heater were deposited on the surface and backside of polycrystalline alumina substrates (dimensions: 2 mm × 2 mm), respectively. The deposition was performed using radiofrequency (RF, 13.56 MHz) magnetron sputtering. The substrate temperature was maintained at 300 °C during sputtering of the contacts and heater to ensure good adhesion between Pt and alumina. The dispersion of InS was then drop-cast onto alumina substrates using a Gilson dispenser (Gilson Company, Inc., USA). Sensing measurements of the material toward different gases were performed in a thermostatic chamber, where the humidity level was controlled using a humidity sensor. Gas tests were performed using a flow-through technique. A detailed description of the systems used for gas-sensing investigations has been reported previously.[68] Before starting the measurements of the fabricated InS sensors under the flow of different gaseous compounds, their baseline electrical conductance was stabilized in air for 10 h at each operating temperature. The response values of InS to oxidizing gaseous compounds were calculated according to:[68]

$$S = \frac{(R_f - R_0)}{R_0} = \frac{\Delta R}{R_0} \quad (3)$$

Herein, R_0 is the baseline electrical resistance of the sensing structure in air, and R_f is the steady state value of its resistance in the presence of the analyte. The response to the reducing gases was calculated as follows:

$$S = \frac{(G_f - G_0)}{G_0} = \frac{\Delta G}{G_0} \quad (4)$$

Here, G_0 is the conductance of the sensor in air, and G_f is the steady-state conductance of InS in the presence of gas.

XPS measurements were conducted using an Al Kα X-ray source coupled with a Scienta R3000 hemispherical electron analyzer. *In situ* measurements were employed for the bulk crystal analysis.

We conducted SPEM measurements using a scanning photoelectron microscope at the Elettra Escamicroscopy beamline. In this configuration, a Fresnel zone plate optics system focuses the X-ray beam onto a spot with a diameter of approximately 140 nm. By scanning the sample relative to the focused X-ray beam, we created chemical and topographical maps while simultaneously collecting element-specific photoelectrons.

5 Computational methods

The atomic structure, energetics of various configurations and interactions was studied by DFT using the QUANTUM-ESPRESSO code[69] and the GGA-PBE,[70] van der Waals-like forces correction[71] were also used. For all simulations, we used ultrasoft pseudopotentials.[72] The values of energy cutoffs of 35 Ry and 400 Ry for the plane-wave expansion of the wave functions and the charge density, respectively. Physisorption differential enthalpies were also calculated by the standard formula:

$$\Delta H_{phys} = [E_{subst+mol} - (E_{subst} + E_{mol})],$$

where E_{subst} is the total energy of the substrate and E_{mol} is the energy of the single molecules of selected species in an empty

box. In the case of water adsorption, we only considered the gaseous phase. Decomposition energy is defined as the difference of the oxygen molecule on the surface. For the case of physisorption, we also evaluated differential Gibbs free energy at a given temperature by the formula:

$$\Delta G = \Delta H - T\Delta S,$$

where T is the temperature, and ΔS is the change of entropy of the adsorbed molecule, which was estimated considering the gas-to-liquid transition by the standard formula:

$$\Delta S = \Delta H_{\text{vaporization}}/T,$$

where $\Delta H_{\text{vaporization}}$ is the measured enthalpy of vaporization.

For the simulations of the surface of bulk InS crystal, we used a slab constructed from $3 \times 3 \times 2$ supercells. To imitate the effect of the rigid subsurface part of the bulk crystal, we performed the calculations for fixed lattice parameters obtained from the calculations for the bulk crystal. Only atomic positions were optimized. The details of the simulation of In_2O_{3-x} surface layers were described in the text.

Author contributions

AP and DWB conceived the project. The draft was written by GDO, DWB, and AP. Crystals were grown by CSL, CNK, and AP. Nanosheets were prepared by JO and characterized by GDO. XPS experiments were carried out by MV and GDO. SPEM experiments were carried out by MA, ZM, LG, and GDO. Raman experiments were carried out by CNK and GDO. XRD experiments were carried out by CNK and CSL. Gas-sensing tests were carried out by VG and EC.

Conflicts of interest

There are no conflicts to declare.

Acknowledgements

This work has been supported by the PRIN 2022 (Grant 2022LFWJBR, acronym PLANET) and PRIN PNRR (Grant P20223LXTA, acronym ENTANGLE) projects by the Ministry of University and Research of Italy, under the coordination of AP. AP and GDO acknowledge Elettra Sincrotrone Trieste S.C.p.A. and CERIC-ERIC for supporting costs related to NAP-XPS, SPEM, and TEM experiments. The *in situ* high pressure/temperature Raman apparatus from the National Cheng Kung University's Core Facility Center is acknowledged by the authors.

References

1 C. Badie, J. H. Lee, A. Mirzaei, H. W. Kim, S. Sayegh, M. Bechelany, L. Santinacci and S. S. Kim, *J. Mater. Chem. A*, 2023, **11**, 12202–12213.
2 R. Zhao, Y. Luo, F. Jiang, Y. Dai, Z. Ma, J. Zhong, P. Wu, T. Zhou and Y. Huang, *J. Mater. Chem. A*, 2022, **10**, 7948–7959.
3 J. Yan, X. Guo, Y. Zhu, Z. Song and L. Y. S. Lee, *J. Mater. Chem. A*, 2022, **10**, 15657–15664.
4 C. Wang, L. Yin, L. Zhang, D. Xiang and R. Gao, *Sensors*, 2010, **10**, 2088–2106.
5 N. Barsan, D. Koziej and U. Weimar, *Sens. Actuators, B*, 2007, **121**, 18–35.
6 A. Dey, *Mater. Sci. Eng., B*, 2018, **229**, 206–217.
7 B. Yang, N. V. Myung and T. T. Tran, *Adv. Electron. Mater.*, 2021, **7**, 2100271.
8 L.-X. Ou, M.-Y. Liu, L.-Y. Zhu, D. W. Zhang and H.-L. Lu, *Nano-Micro Lett.*, 2022, **14**, 206.
9 A. Mirzaei, J.-H. Lee, S. M. Majhi, M. Weber, M. Bechelany, H. W. Kim and S. S. Kim, *J. Appl. Phys.*, 2019, **126**, 241102.
10 Z. Zhang, X. Zou, L. Xu, L. Liao, W. Liu, J. Ho, X. Xiao, C. Jiang and J. Li, *Nanoscale*, 2015, **7**, 10078–10084.
11 M. Tang, Z. Wang, D. Wang, R. Mao, H. Zhang, W. Xu, Z. Yang and D. Zhang, *J. Mater. Chem. A*, 2023, **11**, 9942–9954.
12 P. K. Roy, J. Luxa and Z. Sofer, *Nanoscale*, 2020, **12**, 10430–10446.
13 V. Galstyan, A. Moumen, G. W. Kumarage and E. Comini, *Sens. Actuators, B*, 2022, **357**, 131466.
14 S. Yang, C. Jiang and S.-h. Wei, *Appl. Phys. Rev.*, 2017, **4**, 021304.
15 B. Liu, L. Chen, G. Liu, A. N. Abbas, M. Fathi and C. Zhou, *ACS Nano*, 2014, **8**, 5304–5314.
16 C. Anichini, W. Czepa, D. Pakulski, A. Aliprandi, A. Ciesielski and P. Samorì, *Chem. Soc. Rev.*, 2018, **47**, 4860–4908.
17 S. Cui, H. Pu, S. A. Wells, Z. Wen, S. Mao, J. Chang, M. C. Hersam and J. Chen, *Nat. Commun.*, 2015, **6**, 8632.
18 G. D'Olimpio, V. Galstyan, C. Ghica, M. Vorokhta, M. C. Istrate, C. N. Kuo, C. S. Lue, D. W. Boukhvalov, E. Comini and A. Politano, *J. Mater. Chem. A*, 2023, **11**, 12315–12327.
19 Y. Yang, B. Zong, Q. Xu, Q. Li, Z. Li and S. Mao, *Anal. Chem.*, 2023, **95**, 18065–18074.
20 Q. Xu, B. Zong, Y. Yang, Q. Li and S. Mao, *Sens. Actuators, B*, 2022, **373**, 132696.
21 B. Zong, Q. Li, X. Chen, C. Liu, L. Li, J. Ruan and S. Mao, *ACS Appl. Mater. Interfaces*, 2020, **12**, 50610–50618.
22 J. Zhang, F. Lv, Z. Li, G. Jiang, M. Tan, M. Yuan, Q. Zhang, Y. Cao, H. Zheng, L. Zhang, C. Tang, W. Fu, C. Liu, K. Liu, L. Gu, J. Jiang, G. Zhang and S. Guo, *Adv. Mater.*, 2022, **34**, 2105276.
23 P. Waszczuk, A. Wieckowski, P. Zelenay, S. Gottesfeld, C. Coutanceau, J. M. Léger and C. Lamy, *J. Electroanal. Chem.*, 2001, **511**, 55–64.
24 S. Nappini, D. W. Boukhvalov, G. D'Olimpio, L. Zhang, B. Ghosh, C. N. Kuo, H. Zhu, J. Cheng, M. Nardone and L. Ottaviano, *Adv. Funct. Mater.*, 2020, **30**, 2000915.
25 D. W. Boukhvalov, J. Cheng, G. D'Olimpio, F. C. Bocquet, C. N. Kuo, A. B. Sarkar, B. Ghosh, I. Vobornik, J. Fujii, K. Hsu, L. M. Wang, O. Azulay, G. N. Daptary, D. Naveh, C. S. Lue, M. Vorokhta, A. Agarwal, L. Zhang and A. Politano, *J. Phys. Chem. Lett.*, 2021, **12**, 8627–8636.

26 P. Kushwaha, A. Patra, E. Anjali, H. Surdi, A. Singh, C. Gurada, S. Ramakrishnan, S. S. Prabhu, A. V. Gopal and A. Thamizhavel, *Opt. Mater.*, 2014, **36**, 616–620.
27 J. Chandrasekar and D. Manikandan, *AIP Conf. Proc.*, 2023, **2603**, 040001.
28 J. N. Coleman, *Acc. Chem. Res.*, 2013, **46**, 14–22.
29 J. N. Coleman, M. Lotya, A. O'Neill, S. D. Bergin, P. J. King, U. Khan, K. Young, A. Gaucher, S. De, R. J. Smith, I. V. Shvets, S. K. Arora, G. Stanton, H. Y. Kim, K. Lee, G. T. Kim, G. S. Duesberg, T. Hallam, J. J. Boland, J. J. Wang, J. F. Donegan, J. C. Grunlan, G. Moriarty, A. Shmeliov, R. J. Nicholls, J. M. Perkins, E. M. Grieveson, K. Theuwissen, D. W. McComb, P. D. Nellist and V. Nicolosi, *Science*, 2011, **331**, 568–571.
30 O. A. Balitskii, V. P. Savchyn and V. O. Yukhymchuk, *Semicond. Sci. Technol.*, 2002, **17**, L1–L4.
31 T. E. Beechem, B. M. Kowalski, M. T. Brumbach, A. E. McDonald, C. D. Spataru, S. W. Howell, T. Ohta, J. A. Pask and N. G. Kalugin, *Appl. Phys. Lett.*, 2015, **107**, 173103.
32 D. W. Boukhvalov, G. D'Olimpio, S. Nappini, L. Ottaviano, F. Bondino and A. Politano, *Isr. J. Chem.*, 2022, e202100125.
33 P. Tonndorf, S. Schwarz, J. Kern, I. Niehues, O. Del Pozo-Zamudio, A. I. Dmitriev, A. P. Bakhtinov, D. N. Borisenko, N. N. Kolesnikov and A. I. Tartakovskii, *2D Mater.*, 2017, **4**, 021010.
34 H. Yoshida, S. Nakashima and A. Mitsuishi, *Phys. Status Solidi B*, 1973, **59**, 655–666.
35 Y. Fan, X. Ma, X. Liu, J. Wang, H. Ai and M. Zhao, *J. Phys. Chem. C*, 2018, **122**, 27803–27810.
36 S. Lei, L. Ge, S. Najmaei, A. George, R. Kappera, J. Lou, M. Chhowalla, H. Yamaguchi, G. Gupta, R. Vajtai, A. D. Mohite and P. M. Ajayan, *ACS Nano*, 2014, **8**, 1263–1272.
37 Y. Yang, J. Jeon, J. H. Park, M. S. Jeong, B. H. Lee, E. Hwang and S. Lee, *ACS Nano*, 2019, **13**, 8804–8810.
38 Y. Zhao, D. Yu, J. Lu, L. Tao, Z. Chen, Y. Yang, A. Wei, L. Tao, J. Liu and Z. Zheng, *Adv. Opt. Mater.*, 2019, **7**, 1901085.
39 E. Kärber, K. Otto, A. Katerski, A. Mere and M. Krunks, *Mater. Sci. Semicond. Process.*, 2014, **25**, 137–142.
40 N. M. Gasanly, H. Özkan, A. Aydinli and İ. Yilmaz, *Solid State Commun.*, 1999, **110**, 231–236.
41 H.-Y. Wang, X.-F. Li, L. Xu, X.-S. Li and Q.-K. Hu, *Commun. Theor. Phys.*, 2018, **69**, 211.
42 D. Tuschel, *Spectroscopy*, 2014, **29**, 14.
43 A. Nelson, D.-H. Ha and R. D. Robinson, *Chem. Mater.*, 2016, **28**, 8530–8541.
44 Z. M. Detweiler, S. M. Wulfsberg, M. G. Frith, A. B. Bocarsly and S. L. Bernasek, *Surf. Sci.*, 2016, **648**, 188–195.
45 M. Ivanovskaya, A. Gurlo and P. Bogdanov, *Sens. Actuators, B*, 2001, **77**, 264–267.
46 V. Kumar, S. M. Majhi, K.-H. Kim, H. W. Kim and E. E. Kwon, *Chem. Eng. J. (Lausanne)*, 2021, **404**, 126472.
47 K. Inyawilert, A. Wisitsora-at, A. Tuantranont, P. Singjai, S. Phanichphant and C. Liewhiran, *Sens. Actuators, B*, 2014, **192**, 745–754.
48 G. Korotcenkov, S. D. Han, B. K. Cho and V. Brinzari, *Crit. Rev. Solid State Mater. Sci.*, 2009, **34**, 1–17.
49 A. Gurlo, M. Ivanovskaya, N. Bârsan, M. Schweizer-Berberich, U. Weimar, W. Göpel and A. Diéguez, *Sens. Actuators, B*, 1997, **44**, 327–333.
50 J. Occhiuzzi, G. G. Politano, G. D'Olimpio and A. Politano, *Molecules*, 2023, **28**, 1484.
51 G. D'Olimpio, S. Nappini, M. Vorokhta, L. Lozzi, F. Genuzio, T. O. Menteş, V. Paolucci, B. Gürbulak, S. Duman, L. Ottaviano, A. Locatelli, F. Bondino, D. W. Boukhvalov and A. Politano, *Adv. Funct. Mater.*, 2020, **30**, 2005466.
52 P.-H. Ho, Y.-R. Chang, Y.-C. Chu, M.-K. Li, C.-A. Tsai, W.-H. Wang, C.-H. Ho, C.-W. Chen and P.-W. Chiu, *ACS Nano*, 2017, **11**, 7362–7370.
53 I. Miyake, T. Tanpo and C. Tatsuyama, *Jpn. J. Appl. Phys.*, 1984, **23**, 172.
54 B. Hemanth Kumar, S. Shaji and M. C. Santhosh Kumar, *J. Mater. Sci.: Mater. Electron.*, 2019, **30**, 17986–17998.
55 M. Cheng, Z. Wu, G. Liu, L. Zhao, Y. Gao, B. Zhang, F. Liu, X. Yan, X. Liang, P. Sun and G. Lu, *Sens. Actuators, B*, 2019, **291**, 216–225.
56 Y. B. Kim, S. H. Jung, D. S. Kim, N. G. Deshpande, H. W. Suh, H. H. Lee, J. H. Choi, H. S. Lee and H. K. Cho, *Adv. Funct. Mater.*, 2021, **31**, 2102439.
57 Y. Cheng, Z. Li, T. Tang, K. Xu, H. Yu, X. Tao, C. M. Hung, N. D. Hoa, Y. Fang, B. Ren, H. Chen and J. Z. Ou, *Appl. Mater. Today*, 2022, **26**, 101355.
58 G. Lee, S. Kim, S. Jung, S. Jang and J. Kim, *Sens. Actuators, B*, 2017, **250**, 569–573.
59 S. Cui, H. Pu, E. C. Mattson, Z. Wen, J. Chang, Y. Hou, C. J. Hirschmugl and J. Chen, *Anal. Chem.*, 2014, **86**, 7516–7522.
60 A. Govind, P. Bharathi, G. Mathankumar, M. K. Mohan, J. Archana, S. Harish and M. Navaneethan, *Diamond Relat. Mater.*, 2022, **128**, 109205.
61 P. Sowti khiabani, E. Marzbanrad, H. Hassani and B. Raissi, *J. Am. Ceram. Soc.*, 2013, **96**, 2493–2498.
62 S. Shah, S. Han, S. Hussain, G. Liu, T. Shi, A. Shaheen, Z. Xu, M. Wang and G. Qiao, *Ceram. Int.*, 2022, **48**, 12291–12298.
63 S. Park, Y. W. Jung, G. M. Ko, D. Y. Jeong and C. Lee, *Appl. Phys. A: Mater. Sci. Process.*, 2021, **127**, 898.
64 V. Paolucci, G. D'Olimpio, C.-N. Kuo, C. S. Lue, D. W. Boukhvalov, C. Cantalini and A. Politano, *ACS Appl. Mater. Interfaces*, 2020, **12**, 34362–34369.
65 Y. Yang, D. Zhang, D. Wang, Z. Xu and J. Zhang, *J. Mater. Chem. A*, 2021, **9**, 14495–14506.
66 H. Yang, C. Zhu, Q. Wu, X. Li, H. Wang, J. Wan, C. Xie and D. Zeng, *Appl. Surf. Sci.*, 2022, **601**, 154213.
67 S. Rani, M. Kumar, P. Garg, R. Parmar, A. Kumar, Y. Singh, V. Baloria, U. Deshpande and V. N. Singh, *ACS Appl. Mater. Interfaces*, 2022, **14**, 15381–15390.
68 V. Galstyan, A. Ponzoni, I. Kholmanov, M. M. Natile, E. Comini, S. Nematov and G. Sberveglieri, *ACS Sens.*, 2019, **4**, 2094–2100.
69 P. Giannozzi, S. Baroni, N. Bonini, M. Calandra, R. Car, C. Cavazzoni, D. Ceresoli, G. L. Chiarotti, M. Cococcioni, I. Dabo, A. Dal Corso, S. de Gironcoli, S. Fabris, G. Fratesi,

R. Gebauer, U. Gerstmann, C. Gougoussis, A. Kokalj, M. Lazzeri, L. Martin-Samos, N. Marzari, F. Mauri, R. Mazzarello, S. Paolini, A. Pasquarello, L. Paulatto, C. Sbraccia, S. Scandolo, G. Sclauzero, A. P. Seitsonen, A. Smogunov, P. Umari and R. M. Wentzcovitch, *J. Phys.: Condens.Matter*, 2009, **21**, 395502.

70 J. P. Perdew, K. Burke and M. Ernzerhof, *Phys. Rev. Lett.*, 1996, **77**, 3865–3868.

71 V. Barone, M. Casarin, D. Forrer, M. Pavone, M. Sambi and A. Vittadini, *J. Comput. Chem.*, 2009, **30**, 934–939.

72 D. Vanderbilt, *Phys. Rev. B: Condens. Matter Mater. Phys.*, 1990, **41**, 7892–7895.